Journal of Materials Chemistry A

RSC Publishing

PAPER

Self-deposition of Pt nanocrystals on Mn_3O_4 coated carbon nanotubes for enhanced oxygen reduction electrocatalysis†

Cite this: *J. Mater. Chem. A*, 2013, **1**, 7463

Yu-Ping Xiao,‡[ab] Wen-Jie Jiang,‡[ab] Shuo Wan,[c] Xing Zhang,[a] Jin-Song Hu,*[a] Zi-Dong Wei*[b] and Li-Jun Wan[a]

Received 20th January 2013
Accepted 22nd April 2013

DOI: 10.1039/c3ta10298j

www.rsc.org/MaterialsA

Developing catalysts with high electrocatalytic activity for oxygen reduction reaction (ORR) has recently attracted much attention because the sluggish ORR limits the performance and commercialization of current PEMFCs and metal–air batteries as well. Herein, a facile approach was reported to synthesize Mn_3O_4 nanoparticle coated carbon nanotubes (Mn_3O_4/CNTs) and self-deposit well-dispersed Pt nanocrystals on Mn_3O_4/CNTs to obtain Pt/Mn_3O_4/CNTs hybrid catalysts *via in situ* reduction of support matrix with no need of any capping agent and additional reducing agent. As a result of good dispersion of uncapped Pt nanocrystals, interconnected carbon nanotube conductive network, and possible synergetic co-catalytic effect from heterojunction interfaces of Pt nanocrystals and Mn_3O_4, the as-prepared Pt/Mn_3O_4/CNTs hybrid catalysts demonstrated much enhanced electrocatalytic activity for ORR. The reported strategy may inspire the development of new high efficient hybrid electrocatalysts in a cost-effective way with the potential to harness the metal/oxide interaction to improve the performance of catalysts.

1 Introduction

The increasing depletion of traditional energy sources on earth spurred the search for new alternative energy and efficient energy storage. Much effort has been put into the commercialization of proton exchange membrane fuel cells (PEMFCs) and the development of next-generation energy storage devices such as metal–air batteries. In both applications, efficient electrochemical reduction of oxygen is crucial for the performance of the devices. Up to now, Pt nanoparticles supported on carbon substrates (known as Pt/C) are still best commercialized catalysts for oxygen reduction reaction (ORR) and commonly used as cathode catalysts in the state-of-the-art fuel cells, although the high cost and scarcity of Pt as well as the sluggish kinetics of ORR stand in the way of their commercialization. The effective way is to develop the catalysts with enhanced ORR activity at low cost by either improving the structures of Pt-based catalysts to lower Pt content and enhance its catalytic activity or developing non-Pt catalysts with comparable electrochemical performance.[1–3] In the former case, several strategies have been explored, including alloying Pt with other low-cost transition metals such as Fe, Ni, Co, Pd and Cu *etc.*;[4–12] depositing a monolayer of Pt onto other nanoparticles;[13–16] and developing Pt nanostructures with high energy facets or favorable shape,[17–21] and so on. In the latter case, various materials such as non-precious metal composites,[22–27] metal chalcogenides,[28] transition metal oxides,[29,30] and doped carbonaceous materials[31,32] have been recently investigated to pursue the high electrochemical activity for ORR. Recently, experimental and theoretical studies reported that metal oxides support significantly improved electrocatalytic activity and stability of Pt nanoparticles in ORR and methanol oxidation reaction *via* strong metal/oxide interactions.[33–37] Although the remarkable progress has been made in past several years, there is still a gap between the commercial criteria and the cutting-edge catalysts in terms of cost, performance and durability.[1–3] Developing the efficient electrocatalysts for ORR, especially in a cost-effective way, to meet industrial requirements for fuel cells and other energy applications is still challenging.

Herein, we took advantage of carbon nanotubes as three dimensional conductive catalyst matrix and developed a facile

[a]*Key Laboratory of Molecular Nanostructure and Nanotechnology, Beijing National Laboratory for Molecular Sciences, Institute of Chemistry, Chinese Academy of Sciences, Beijing, 100190, P. R. China. E-mail: hujs@iccas.ac.cn; Fax: +86 10 82613929; Tel: +86 10 82613929*

[b]*The State Key Laboratory of Power Transmission Equipment & System Security and New Technology, College of Chemistry and Chemical Engineering, Chongqing University, Chongqing, 400044, P. R. China. E-mail: zdwei@cqu.edu.cn*

[c]*College of Chemistry and Chemical Engineering, Xiamen University, Xiamen, 361005, P. R. China*

† Electronic supplementary information (ESI) available: XRD pattern of pure carbon nanotubes, EDS spectra of Mn_3O_4/CNTs and Pt/Mn_3O_4/CNTs, and size distribution histogram of Pt nanocrystals in Pt/Mn_3O_4/CNTs. See DOI: 10.1039/c3ta10298j

‡ These authors contributed equally.

approach for synthesizing Mn_3O_4 nanoparticles coated carbon nanotubes (Mn_3O_4/CNTs) and self-depositing Pt nanocrystals on Mn_3O_4/CNTs to prepare Pt/Mn_3O_4/CNTs hybrid catalysts. The merits of the reported approach are: (1) the catalysts were prepared under mild conditions; (2) well-dispersed Pt nanocrystals with an average size of 2.05 nm directly grew on Mn_3O_4/CNTs *via in situ* reduction of support matrix with no need of any capping agent or additional reducing agent; (3) the as-prepared Pt/Mn_3O_4/CNTs hybrid catalysts demonstrated the enhanced electrocatalytic activity for ORR as a result of good dispersion of uncapped Pt nanocrystals, interconnected carbon nanotube conductive network support, and possible synergetic co-catalytic effect from heterojunction interfaces of Pt nanocrystals and Mn_3O_4.

2 Experimental

Chemicals and materials

N,*N*-Dimethylformamide (DMF), $C_4H_6MnO_4\cdot 4H_2O$, K_2PtCl_4, HNO_3, were obtained from Beijing Chemical Reagent Ltd. and were used without further purification. Carbon nanotubes (CNTs, Shenzhen Nanotech Port Co. Ltd.) were refluxed in concentrated nitric acid for 3 h before experiments.

Synthesis of Mn_3O_4/CNTs composite

19 mg CNTs and 40 mL DMF were mixed together in a flask and ultrasonicated for 1 h, followed by the addition of 0.4 mL manganese acetate (150 mg mL^{-1}). The flask was then heated to 80 °C under stirring for another hour.

Synthesis of Pt/Mn_3O_4/CNTs composite

20 mL ultra-pure water and 0.4 mL K_2PtCl_4 (20 mg mL^{-1}) were added to 20 mL of as-prepared Mn_3O_4/CNTs dispersion in DMF. After stirring at 70 °C for 2 h, the mixture was centrifuged and washed with water and ethanol for several times and dispersed in ethanol solution.

Structural characterization

The morphologies of the catalysts were examined by scanning electron microscopy (Hitachi S-4800, Japan) operated at 15 kV and tunneling electron microscopy JEOL-2010 (JEOL, Japan) working at an accelerating voltage of 200 kV. High-resolution TEM (HRTEM) and high-angle annular dark-field scanning TEM (HAADF-STEM) experiments were performed on a FEI transmission electron microscope (Technai G2 F20) operating at 200 kV. Powder X-ray diffraction (XRD) pattern was carried out with a Regaku D/Max-2500 diffractometer equipped with a Cu Kα1 radiation ($\lambda = 1.54056$ Å). The catalyst loading in terms of Pt content was measured *via* an inductively coupled plasma emission spectrometer (ICP-AES, Shimadzu).

Electrochemical measurements

All electrochemical measurements were carried out on a Potentiostats-Electrochemistry Workstation (PARSTAT 2273A, Princeton Applied Research, TN, USA). A standard three-electrode cell system was used with a catalyst modified glassy carbon (GC) electrode as the work electrode, a saturated calomel electrode (SCE) as reference electrode and a Pt foil as counter electrode. Rotating disk electrode (RDE) test was performed on Radiometer Analytical's RDE electrode (EDI101) in 0.1 M $HClO_4$ with a glassy carbon disk (3 mm in diameter). All measurements were done at room temperature. For preparation of working electrode, a certain amount of catalyst paste with given loading of catalyst was drop-casted on pretreated GC electrode. After drying the electrode at room temperature, 3 μL of 0.1 wt% Nafion (Sigma-Aldrich) in ethanol was spread on the surface of catalysts and dried in air. Before the electrochemical measurements, the catalyst modified working electrodes were first cycled between 0 V and 1.2 V (*vs.* RHE) in N_2-purged 0.1 M $HClO_4$ to produce a clean electrode surface.

CV measurements were performed by cycling the potential between 0 V and 1.2 V (*vs.* RHE) with sweep rate of 50 mV s^{-1} in N_2-purged 0.1 M $HClO_4$ at room temperature. The electrochemical surface areas (ECSA) of catalysts by measuring the charge associated with hydrogen adsorption between 0.05 and 0.37 V (*vs.* RHE (Revisable Hydrogen Electrode)) after double-layer correction and assuming a value of 0.21 mC cm^{-2} for the adsorption of a hydrogen monolayer, corresponding to a surface density of 1.3×10^{15} Pt atoms per cm^2, which is generally accepted for polycrystalline Pt electrodes. ECSA was measured for each catalyst-modified electrode for oxygen reduction experiments.

The electrocatalytic activity for ORR of catalysts was measured on EDI101 RDE with 3 mm GC disk in O_2-saturated 0.1 M $HClO_4$ aqueous solution. The polarization curves were collected by sweeping the potential from 0 V to 1.2 V (*vs.* RHE) at the scan rate of 5 mV s^{-1} and rotation rate of 1600 rpm, and then normalized in reference to the geometric area of the GC RDE (0.07065 cm^2). The loading of catalysts was adjusted to make the recorded current density reach the diffusion limited current density of ~6 mA cm^{-2} and mass-transport would not be an issue in these measurements. The real ECSA and mass loading of Pt was calculated as mentioned above. The kinetic current density (i_k), which is independent of diffusion and could be used to evaluate the intrinsic activity of the catalysts, was calculated on the basis of the measured current density and the Koutecky–Levich equation:

$$\frac{1}{i} = \frac{1}{i_k} + \frac{1}{i_d} = \frac{1}{i_k} + \frac{1}{B\omega^{1/2}}$$

$$B = 0.62nFC_0 D_0^{2/3} \nu^{-1/6}$$

where, i is the measured current density, i_k is the kinetic current density, i_d is the diffusion limited current density, B is a constant as a function of the concentration, diffusion coefficient of O_2 in the electrolyte and viscosity of the electrolyte, n is the number of electrons transferred in the reaction, F is the Faraday constant (96 500 C mol^{-1}), and ω is the rotation rate of the electrode in unit of rad s^{-1}. The area-specified current density (i_k) was obtained by normalizing the current based on ECSA of the catalysts. Mass activity and specific activity for ORR was calculated through dividing kinetic current density obtained at given potential by ECSA and mass of the used catalysts, respectively.

3 Results and discussion

Mn_3O_4/CNTs were prepared *via* the hydrolysis of manganese acetate on the functionalized carbon nanotubes. In briefly, carbon nanotubes were pre-treated in nitric acid to functionalize their surfaces and dispersed in *N*,*N*-dimethylformamide (DMF). Manganese acetate solution was then added into dispersion and the mixture was stirred at 80 °C for 1 hour, which results in the growth of Mn_3O_4 nanoparticles on top of the CNT surfaces under the anchoring of –COOH and –OH groups. In order to obtain Pt/Mn_3O_4/CNTs composites, K_2PtCl_4 was subsequently added into the as-prepared Mn_3O_4/CNTs dispersion and reacted with Mn_3O_4 for 2 hours at 70 °C to *in situ* form Pt nanocrystals on the surface of Mn_3O_4/CNTs. The formation of Pt could be ascribed to the galvanic replacement reaction between $PtCl_4^{2-}$ and Mn_3O_4, probably following the equation according to the literature:[38,39]

$$PtCl_4^{2-} + 2Mn_3O_4(s) + H_2O \rightarrow Pt + 3Mn_2O_3(s) + 2H^+ + 4Cl^-$$

The typical overall platinum loading in Pt/Mn_3O_4/CNTs composite used in the following experiments was 13 wt%, measured by Inductively Coupled Plasma Atomic Emission Spectroscopy (ICP-AES).

The synthesized Mn_3O_4/CNTs and Pt/Mn_3O_4/CNTs were first characterized by powder X-ray diffraction experiment (XRD). As shown in Fig. 1, all major peaks in XRD pattern of the composites obtained without the addition of K_2PtCl_4 (pattern b) can be well indexed to the diffraction from the corresponding crystallographic planes of tetragonal Mn_3O_4 phase (pattern a, JCPDS Card no. 24-0734), except for the strong peak at 26.6° which can be attributed to (003) plane of graphitic carbon nanotubes (Fig. S1,† JCPDS Card no. 26-1079). The result indicates the composite is composed of tetragonal Mn_3O_4 and carbon nanotubes. The XRD pattern of the product collected after the addition of K_2PtCl_4 (pattern c) shows similar features except for a weak wide peak at around 39.5°, which means the product retains the nature of the tetragonal Mn_3O_4 and carbon nanotubes. The additional wide peak at around 39.5° is consistent with the strongest diffraction peak of cubic Pt (JCPDS 04-0802), implying the possible existence of metallic Pt.

The morphologies and composition of the synthesized Mn_3O_4/CNTs and Pt/Mn_3O_4/CNTs were further investigated by transmission electron microscopy (TEM) and scanning electron microscopy (SEM) and equipped with energy dispersive X-ray detector. Compared to TEM image of pure carbon nanotubes (Fig. 2a), the typical TEM image of Mn_3O_4/CNTs (Fig. 2b) clearly shows that the entire surface of the carbon nanotubes are uniformly coated with a large number of nanoparticles in a size of less than 10 nm. Energy Dispersive X-ray Spectrometry (EDS) result confirms that the product is composed of element C, Mn and O (Fig. S2†). Fig. 2c presents a typical SEM image of Pt/Mn_3O_4/CNTs, indicating the composites have rough surfaces instead of smooth surface of pure carbon nanotubes. EDS spectrum confirms the introduction of Pt besides element C, Mn and O (Fig. S3†). A high magnification SEM image (Fig. 2d) displays that a layer of nanoparticles grows on the surfaces of carbon nanotubes. Low-magnification TEM image shown in Fig. 3a indicates Pt/Mn_3O_4/CNTs appears in a morphology similar to Mn_3O_4/CNTs. Plenty of nanoparticles are well dispersed and form a coating layer on carbon nanotubes. More details are revealed in high-magnification TEM image (Fig. 3b). The apparent contrast difference indicate that there are larger nanoparticles in a size of 10–20 nm on the surface of CNT and a lot of small nanodots with darker contrast decorated on the larger nanoparticles. The typical high-resolution TEM images (Fig. 3c and d) clearly displayed the graphite layers of carbon nanotubes as well as the lattice fringes of these larger nanoparticles and small nanodots. The distance of 0.277 nm between adjacent lattice fringes of larger nanoparticles matches well with the *d* spacing of (103) plane of tetragonal Mn_3O_4, while the distance of 0.226 nm for small darker nanodots is in good agreement with *d* spacing of (111) planes of face-centered cubic

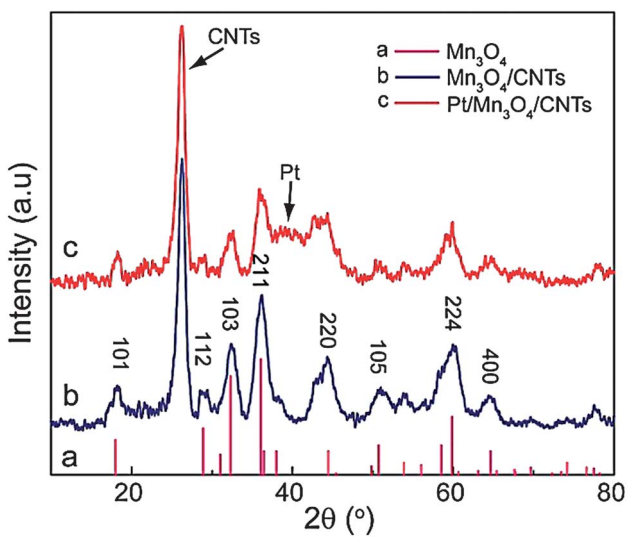

Fig. 1 XRD patterns of Mn_3O_4 (a), Mn_3O_4/CNTs (b) and Pt/Mn_3O_4/CNTs (c).

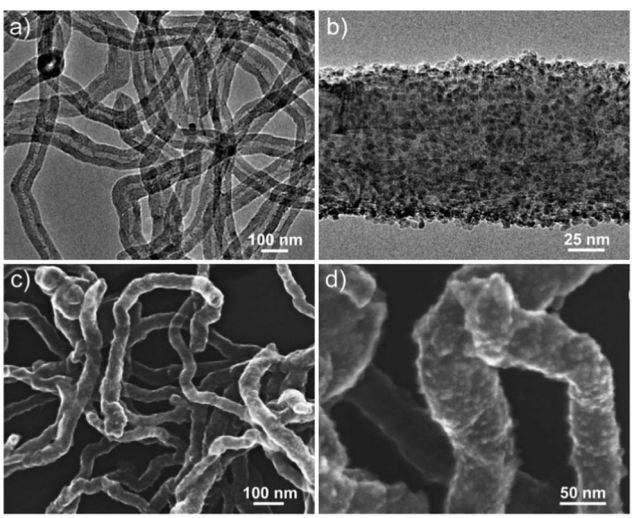

Fig. 2 (a) TEM image of pure carbon nanotubes. (b) TEM image of Mn_3O_4/CNTs. (c and d) SEM images of Pt/Mn_3O_4/CNTs.

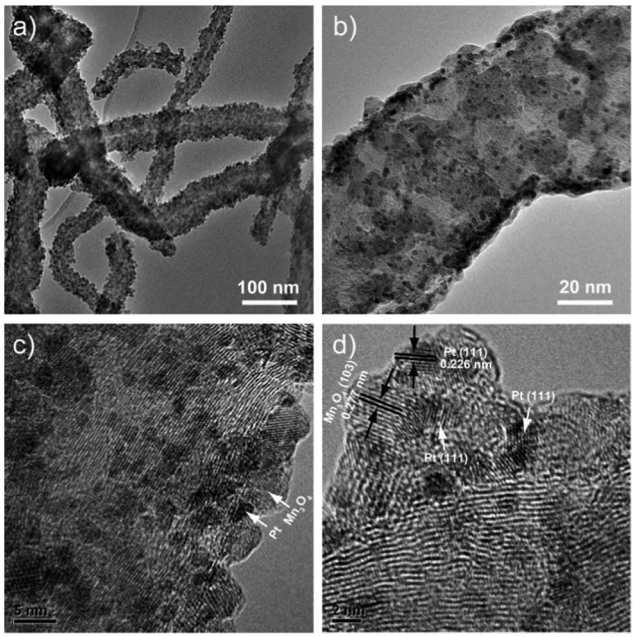

Fig. 3 (a and b) Low-magnification TEM images of $Pt/Mn_3O_4/CNTs$. (c and d) HRTEM images of $Pt/Mn_3O_4/CNTs$.

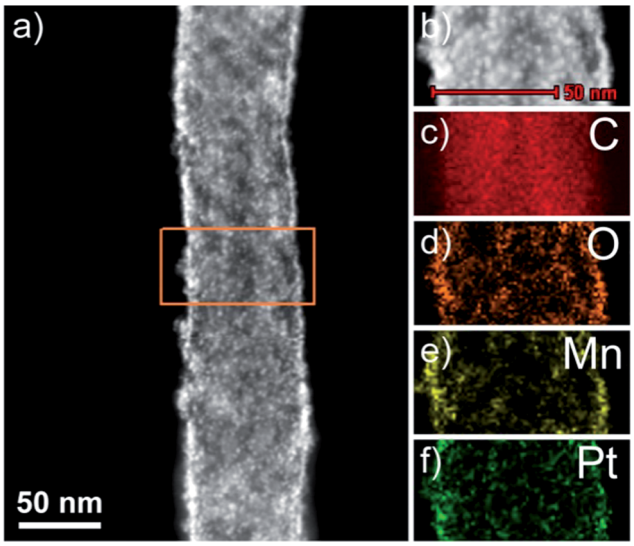

Fig. 4 (a and b) HAADF-STEM image of $Pt/Mn_3O_4/CNTs$. (c–f) Elemental mapping of the selected part shown in (b).

(fcc) crystalline Pt, indicating they are Pt nanocrystals. The average size of these nanocrystals was measured to be 2.05 nm, based on statistical analysis on 100 nanocrystals. The size distribution histogram is shown in Fig. S4.† By comparing Fig. 2b and 3b, it was noted that the morphologies of Mn_3O_4 nanoparticles in $Pt/Mn_3O_4/CNTs$ were slightly different from that in $Mn_3O_4/CNTs$. Mn_3O_4 nanoparticles of less than 10 nm in $Mn_3O_4/CNTs$ composites tend to fuse into larger irregular particles after reacting with $PtCl_4^{2-}$ at 70 °C for 2 h. These particles seem in closer contact with the surface of CNT and Pt nanocrystals apparently deposited on top of these particles rather than the CNT surface, which supports the fact that Mn_3O_4 reduces $PtCl_4^{2-}$ to form Pt nanocrystals on its top.

The high-angle annular dark-field scanning TEM (HAADF-STEM) imaging technique was used to further investigate the composition and structure of the prepared $Pt/Mn_3O_4/CNTs$ composites. It is known that contrast variations in HAADF-STEM images are proportional to the square of the element's atomic number and can therefore provide important information regarding the elemental distribution within nanostructures at sub-angstrom resolution. Fig. 4a is a typical HAADF-STEM image of a part of a single $Pt/Mn_3O_4/CNTs$ composite, clearly showing there are a plenty of bright spots in a similar size of around 2 nm uniformly decorated on the surface of CNT composite with no obvious aggregation. Combining the above-mentioned TEM, XRD, and EDS results, these bright spots can be easily ascribed to Pt nanocrystals. The EDS analysis on the area marked with orange frame in Fig. 4a confirms the composite is only composed of the element C, O, Mn, and Pt, and elemental mapping results shown in Fig. 4c–f reveal the distribution of each element in the composite, which perfectly match the positions as indicated in TEM and STEM images.

Developing catalysts with high electrocatalytic ORR activity has recently attracted much attention because it is known that oxygen reduction reaction is six or more orders of magnitude slower than the anode hydrogen oxidation reaction in current PEMFCs and thus limits cell performance. Since PEMFCs commonly run in acidic media, the electrocatalytic performance of the synthesized $Mn_3O_4/CNTs$ and $Pt/Mn_3O_4/CNTs$ was accessed by measuring their ORR activities in acidic conditions instead of alkaline conditions and benchmarking against a commercial Pt/C catalyst (Johnson-Matthey, 20 wt% Pt).

Pt/Mn_3O_4 was also prepared with the same procedure as $Pt/Mn_3O_4/CNTs$ but without CNT support for comparison. In order to calculate the electrochemical surface areas (ECSA) and thus the specific ORR activities of catalysts, the cyclic voltammetry (CV) curves of the catalysts were first recorded before ORR measurement at room temperature in an N_2-purged 0.1 M $HClO_4$ solution with a sweep rate of 50 mV s^{-1}. As shown in Fig. 5a, each CV curves exhibit strong peaks associated with the adsorption/desorption of hydrogen and the formation/reduction of Pt oxides. ECSA were calculated by measuring the charge associated with the H_{ads} (Q_H) between 0.05 and 0.37 V (*vs.* RHE) and assuming $Q_{ref} = 0.21$ mC cm^{-2} for the adsorption of a hydrogen monolayer, corresponding to a surface density of 1.3×10^{15} Pt atoms per cm^2, which is generally accepted for polycrystalline Pt electrodes. The specific ECSA of the as-prepared $Pt/Mn_3O_4/CNTs$ was 94.4 $m^2\ g^{-1}$, which is comparable of that of commercial Pt/C catalyst (94.5 $m^2\ g^{-1}$) but ~2.5 times that of Pt/Mn_3O_4 (37.4 $m^2\ g^{-1}$). ORR experiments were carried out in oxygen-saturated 0.1 M $HClO_4$ by using a catalysts-coated glassy carbon rotating disk electrode (RDE) as working electrode at room temperature. Fig. 5b shows typical ORR polarization curves of $Pt/Mn_3O_4/CNTs$, Pt/Mn_3O_4, and commercial Pt/C catalysts, which were recorded at an RDE rotation speed of 1600 rpm. It can be seen that $Pt/Mn_3O_4/CNTs$ exhibited more positive onset potential and half-wave potential compared to Pt/C and Pt/Mn_3O_4, indicating the higher catalytic activity of $Pt/Mn_3O_4/CNTs$ for ORR. The kinetic current density (i_k) was further

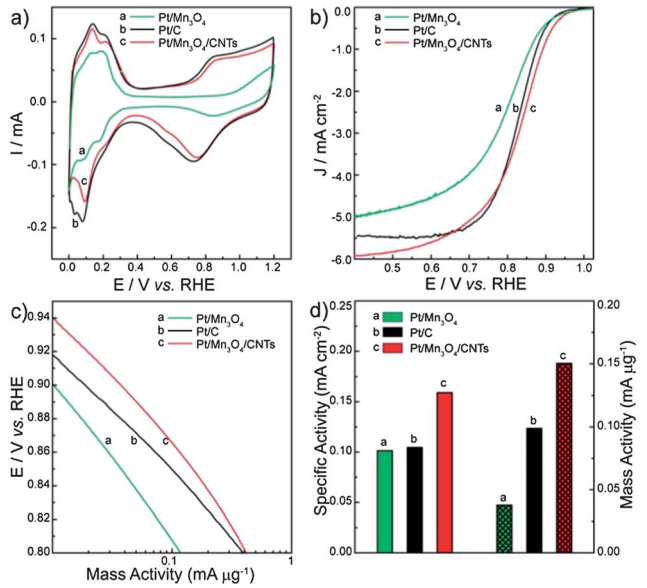

Fig. 5 Comparison of electrocatalytic properties of $Pt/Mn_3O_4/CNTs$, Pt/Mn_3O_4, and commercial Pt/C catalyst (Johnson-Matthey) (20% by weight of Pt nanoparticles on carbon support). (a) CV curves recorded at room temperature in an N_2-purged 0.1 M $HClO_4$ solution with a sweep rate of 50 mV s^{-1}. (b) ORR polarization curves for $Pt/Mn_3O_4/CNTs$, Pt/Mn_3O_4, and Pt/C catalyst recorded at room temperature in an O_2-saturated 0.1 M $HClO_4$ solution with a sweep rate of 5 mV s^{-1} and a rotation rate of 1600 rpm. (c) Kinetic current density for three catalysts normalized to the metal loading at low overpotential. (d) Mass activity and ECSA specific activity at 0.85 V *versus* RHE for these three catalysts. Mass and specific activities are given as kinetic current densities normalized in reference to the loading amount and ECSA of Pt, respectively.

calculated by using Koutecky–Levich equation to represent the intrinsic activity of the catalysts. Fig. 5c presents the kinetic current for three catalysts normalized to the metal loading at low overpotential. $Pt/Mn_3O_4/CNTs$ delivered the higher mass-specific kinetic current than Pt/C and Pt/Mn_3O_4 at same potential. Furthermore, ECSA specific activity and mass activity of three catalysts were also calculated based on the kinetic current density obtained at 0.85 V. As shown in Fig. 5d, $Pt/Mn_3O_4/CNTs$ manifested the highest specific activity (0.16 mA cm_{Pt}^{-2}) and mass activity (0.15 mA μg_{Pt}^{-1}), which are 1.6 times, 1.5 times those for Pt/C catalyst, and 1.6 times, 3.97 times those for Pt/Mn_3O_4, respectively. Given the fact that the electrochemical performance of $Pt/Mn_3O_4/CNTs$ for ORR is also better than that of Pt nanoparticles on CNTs reported in the literature,[40] this improvement could be attributed to good distribution of Pt nanocrystals on support, high surface area and the formation of interconnected carbon nanotube conductive network, as well as the possible synergetic co-catalytic effect at the heterojunction interfaces formed between Pt nanocrystals and Mn_3O_4 support.[33–36] The electrocatalytic activity could be further enhanced by optimizing the size of Pt nanocrystals and Pt content in $Pt/Mn_3O_4/CNTs$.

4 Conclusions

In summary, we report a new facile approach for synthesizing $Pt/Mn_3O_4/CNTs$ composite catalysts. Compared to the traditional methods for synthesizing metal, CNTs, and/or metal oxide composites, the reported $Pt/Mn_3O_4/CNTs$ were prepared under mild conditions with no introduction of any organic capping agent or additional reducing agent. Well-dispersed Pt nanocrystals in a size of *ca.* 2 nm were deposited on the surface of $Mn_3O_4/CNTs$ *via* its own reduction capability. By combining the advantages from uncapped and well-dispersed Pt nanocrystals, the interconnected carbon nanotube conductive network, and the possible synergetic co-catalytic effect from heterojunction interfaces of Pt nanocrystals and Mn_3O_4 support, the prepared $Pt/Mn_3O_4/CNTs$ demonstrated much enhanced electrocatalytic activity for ORR.

Acknowledgements

This work was supported by the National Natural Science Foundation of China (Grants nos 91127044, 21173237, and 21121063), the National Key Project on Basic Research (Grants no. 2009CB930400 and 2011CB808700), and the Chinese Academy of Sciences.

Notes and references

1 M. K. Debe, *Nature*, 2012, **486**, 43–51.
2 A. Rabis, P. Rodriguez and T. J. Schmidt, *ACS Catal.*, 2012, **2**, 864–890.
3 H. Yang, *Angew. Chem., Int. Ed.*, 2011, **50**, 2674–2676.
4 C. Wang, N. M. Markovic and V. R. Stamenkovic, *ACS Catal.*, 2012, **2**, 891–898.
5 B. Lim, M. J. Jiang, P. H. C. Camargo, E. C. Cho, J. Tao, X. M. Lu, Y. M. Zhu and Y. N. Xia, *Science*, 2009, **324**, 1302–1305.
6 V. R. Stamenkovic, B. Fowler, B. S. Mun, G. F. Wang, P. N. Ross, C. A. Lucas and N. M. Markovic, *Science*, 2007, **315**, 493–497.
7 L. Wang, Y. Nemoto and Y. Yamauchi, *J. Am. Chem. Soc.*, 2011, **133**, 9674–9677.
8 J. I. Shui, C. Chen and J. C. M. Li, *Adv. Funct. Mater.*, 2011, **21**, 3357–3362.
9 L. F. Liu and E. Pippel, *Angew. Chem., Int. Ed.*, 2011, **50**, 2729–2733.
10 C. Koenigsmann, A. C. Santulli, K. P. Gong, M. B. Vukmirovic, W. P. Zhou, E. Sutter, S. S. Wong and R. R. Adzic, *J. Am. Chem. Soc.*, 2011, **133**, 9783–9795.
11 D. F. Yancey, E. V. Carino and R. M. Crooks, *J. Am. Chem. Soc.*, 2010, **132**, 10988–10989.
12 Z. M. Peng and H. Yang, *J. Am. Chem. Soc.*, 2009, **131**, 7542–7543.
13 D. F. van der Vliet, C. Wang, D. G. Li, A. P. Paulikas, J. Greeley, R. B. Rankin, D. Strmcnik, D. Tripkovic, N. M. Markovic and V. R. Stamenkovic, *Angew. Chem., Int. Ed.*, 2012, **51**, 3139–3142.
14 C. Wang, M. F. Chi, D. G. Li, D. Strmcnik, D. van der Vliett, G. F. Wang, V. Komanicky, K. C. Chang, A. P. Paulikas, D. Tripkovic, J. Pearson, K. L. More, N. M. Markovic and V. R. Stamenkovic, *J. Am. Chem. Soc.*, 2011, **133**, 14396–14403.

15 J. Zhang, K. Sasaki, E. Sutter and R. R. Adzic, *Science*, 2007, **315**, 220–222.
16 J. X. Wang, H. Inada, L. J. Wu, Y. M. Zhu, Y. M. Choi, P. Liu, W. P. Zhou and R. R. Adzic, *J. Am. Chem. Soc.*, 2009, **131**, 17298–17302.
17 H. X. Liu, N. Tian, M. P. Brandon, Z. Y. Zhou, J. L. Lin, C. Hardacre, W. F. Lin and S. G. Sun, *ACS Catal.*, 2012, **2**, 708–715.
18 Y. J. Deng, N. Tian, Z. Y. Zhou, R. Huang, Z. L. Liu, J. Xiao and S. G. Sun, *Chem. Sci.*, 2012, **3**, 1157–1161.
19 N. Tian, Z. Y. Zhou, S. G. Sun, Y. Ding and Z. L. Wang, *Science*, 2007, **316**, 732–735.
20 B. Y. Xia, W. T. Ng, H. B. Wu, X. Wang and X. W. Lou, *Angew. Chem., Int. Ed.*, 2012, **51**, 7213–7216.
21 J. B. Wu, L. Qi, H. J. You, A. Gross, J. Li and H. Yang, *J. Am. Chem. Soc.*, 2012, **134**, 11880–11883.
22 Z. W. Chen, D. Higgins, A. P. Yu, L. Zhang and J. J. Zhang, *Energy Environ. Sci.*, 2011, **4**, 3167–3192.
23 F. Sedona, M. Di Marino, D. Forrer, A. Vittadini, M. Casarin, A. Cossaro, L. Floreano, A. Verdini and M. Sambi, *Nat. Mater.*, 2012, **11**, 970–977.
24 J. Suntivich, H. A. Gasteiger, N. Yabuuchi, H. Nakanishi, J. B. Goodenough and Y. Shao-Horn, *Nat. Chem.*, 2011, **3**, 546–550.
25 F. Y. Cheng, J. A. Shen, B. Peng, Y. D. Pan, Z. L. Tao and J. Chen, *Nat. Chem.*, 2011, **3**, 79–84.
26 G. Wu, K. L. More, C. M. Johnston and P. Zelenay, *Science*, 2011, **332**, 443–447.
27 D. Deng, L. Yu, X. Chen, G. Wang, L. Jin, X. Pan, J. Deng, G. Sun and X. Bao, *Angew. Chem., Int. Ed.*, 2013, **52**, 371–375.
28 H. L. Wang, Y. Y. Liang, Y. G. Li and H. J. Dai, *Angew. Chem., Int. Ed.*, 2011, **50**, 10969–10972.
29 Y. Y. Liang, H. L. Wang, J. G. Zhou, Y. G. Li, J. Wang, T. Regier and H. J. Dai, *J. Am. Chem. Soc.*, 2012, **134**, 3517–3523.
30 Y. Y. Liang, Y. G. Li, H. L. Wang, J. G. Zhou, J. Wang, T. Regier and H. J. Dai, *Nat. Mater.*, 2011, **10**, 780–786.
31 R. L. Liu, D. Q. Wu, X. L. Feng and K. Müllen, *Angew. Chem., Int. Ed.*, 2010, **49**, 2565–2569.
32 Y. G. Li, W. Zhou, H. L. Wang, L. M. Xie, Y. Y. Liang, F. Wei, J. C. Idrobo, S. J. Pennycook and H. J. Dai, *Nat. Nanotechnol.*, 2012, **7**, 394–400.
33 B. R. Camacho, C. Morais, M. A. Valenzuela and N. Alonso-Vante, *Catal. Today*, 2013, **202**, 36–43.
34 G. N. Vayssilov, Y. Lykhach, A. Migani, T. Staudt, G. P. Petrova, N. Tsud, T. Skala, A. Bruix, F. Illas, K. C. Prince, V. Matolin, K. M. Neyman and J. Libuda, *Nat. Mater.*, 2011, **10**, 310–315.
35 T. T. H. Van, C. J. Pan, J. Rick, W. N. Su and B. J. Hwang, *J. Am. Chem. Soc.*, 2011, **133**, 11716–11724.
36 R. Kou, Y. Y. Shao, D. H. Mei, Z. M. Nie, D. H. Wang, C. M. Wang, V. V. Viswanathan, S. Park, I. A. Aksay, Y. H. Lin, Y. Wang and J. Liu, *J. Am. Chem. Soc.*, 2011, **133**, 2541–2547.
37 X. L. Yang, X. Y. Wang, G. Q. Zhang, J. P. Zheng, T. S. Wang, X. Z. Liu, Ch. Y. Shu, L. Jiang and C. R. Wang, *Int. J. Hydrogen Energy*, 2012, **37**, 11167–11175.
38 K. W. Kim, S. M. Kim, S. Choi, J. Kim and I. S. Lee, *ACS Nano*, 2012, **6**, 5122–5129.
39 X. Z. Gong, Y. Yang and S. M. Huang, *Chem. Commun.*, 2011, **47**, 1009–1011.
40 S. Zhang, Y. Y. Shao, G. P. Yin and Y. H. Lin, *J. Mater. Chem.*, 2010, **20**, 2826–2830.

